Springer

KSME

Journal of Mechanical Science and Technology 25 (2) (2011) 457~467
www.springerlink.com/content/1738-494x
DOI 10.1007/s12206-010-1229-z

# A numerical study on the performance of polymer electrolyte membrane fuel cells due to the variation in gas diffusion layer permeability †

Seung Man Baek[1], Soo Gon Koh[2], Kwang Nam Kim[1], Jung Ho Kang[1], Jin Hyun Nam[3] and Charn-Jung Kim[1,*]

[1]*School of Mechanical and Aerospace Engineering, Seoul National University, Seoul, 151-742, Korea*
[2]*Computational Analysis Team, Mando Corporation,Gangwon, 220-805, Korea*
[3]*School of Automotive, Industrial, and Mechanical Engineering, Daegu University, Gyungsan, 712-714, Korea*

(Manuscript Received April 26, 2010; Revised November 6, 2010; Accepted November 22, 2010)

**Abstract**

Convective flow in the under-rib regions of gas diffusion layers (GDLs) is a non-negligible transport process that can enhance the performance of polymer electrolyte membrane fuel cells (PEMFCs) by facilitating efficient utilization of catalyst layers (CLs) in those regions. The permeability of GDLs has been recognized as a dominant factor influencing the intensity of the under-rib convection in PEMFCs. In this study, the correlation between the permeability of GDLs and the performance of PEMFCs was numerically investigated through a detailed simulation of the transport and electrochemical processes in PEMFCs using a computational fluid dynamics (CFD) tool. Three serpentine flow fields with one, three, or five parallel paths were considered as reactant flow channels for an active cell area of 3 cm × 3 cm, while the permeability of GDLs was varied from $1\times10^{-12}$ $m^2$ to $1\times10^{-10}$ $m^2$. The effects of the flow field design and the GDL permeability on the performance of PEMFCs were presented, along with their impacts on the local distribution of current density, water content, and reactant concentration.

*Keywords*: Polymer electrolyte membrane fuel cell; Gas diffusion layer; Permeability; Under-rib convection

## 1. Introduction

Polymer electrolyte membrane fuel cells (PEMFCs) have been studied extensively as power sources for portable electronic devices and transportation vehicles due to their high efficiency, clean emissions, and low operating temperatures [1, 2]. Recently, research efforts have been directed to improving the performance of PEMFCs through system-level design and operation optimization, e.g., better management of water and heat [3-5] or better design of reactant and coolant flow fields [6-9].

In this regard, the convective flow through under-rib regions of gas diffusion layers (GDLs), or so-called under-rib convection, has received much research attention as a possible route towards an improved performance of PEMFCs. The under-rib convection is an essential transport process for interdigitated flow fields with dead-end channel designs [10, 11]. In addition, the under-rib convection is also found to be important for serpentine flow fields with long channel lengths [12-14].

A relatively large pressure difference develops between adjacent gas channels (GCs) in serpentine flow fields during the operation of PEMFCs, which leads to an increased leakage or by-pass flow rate through the under-rib paths. The permeability of GDLs has been recognized as the crucial factor that determines the intensity of the under-rib convection for PEMFCs with serpentine flow fields [15-17]. Pharoah [16] showed that the convective transport through under-rib regions became non-negligible when the permeability of GDLs exceeds $10^{-13}$ $m^2$. In fact, most of GDL materials currently used in PEMFCs have permeabilities higher than $10^{-13}$ $m^2$ [15, 17].

It has been reported that the under-rib convection in serpentine flow fields can improve the performance of PEMFCs by increasing the reactant concentration in catalyst layers (CLs) and facilitating the water transport in GDLs [18, 19]. Higher under-rib convection was also found to result in more uniform concentration of methanol for direct methanol fuel cells (DMFCs) with serpentine flow fields [20]. In addition, Xu and Zhao [6] experimentally have shown that a convection-enhanced serpentine flow field (CESFF) results in better performance and more stable operation of DMFCs.

Thus, the under-rib convection is believed to allow more ef-

† This paper was recommended for publication in revised form by Associate Editor Tong Seop Kim

* Corresponding author. Tel.: +82 2 880 1662, Fax.: +82 2 883 0179
E-mail address: kimcj@snu.ac.kr

fective utilization of electrocatalysts in CLs by increasing the reactant concentration, and also to enable more efficient removal of liquid water from GDLs. And this in turn enhances the performance of PEMFCs with serpentine flow fields. However, under-rib convection is believed to be negligible for parallel flow fields, mainly due to the relatively small pressure difference between adjacent GCs. Ahmed et al. [21] showed that the performance of PEMFCs with parallel flow fields was improved only slightly when the permeability of GDLs was increased.

In this study, computational fluid dynamics (CFD) simulation was used to investigate the correlation between the permeability of GDLs and the performance of PEMFCs. Three serpentine flow fields with one, three, or five parallel paths were considered as reactant GCs to inspect the effects of the under-rib convection in different flow field designs. In the CFD simulation, the permeability of GDLs was varied by 100-fold, from $1\times10^{-12}$ $m^2$ to $1\times10^{-10}$ $m^2$. The effects of the flow field design and the GDL permeability on the performance of PEMFCs were presented, along with their impacts on the local distribution of current density, water content, and reactant concentration.

Table 1. Geometrical model parameters.

| Parameter | Value |
|---|---|
| Channel height | 0.8 mm |
| Channel width | 1.0 mm |
| Rib width | 1.0 mm |
| Active cell area | 3 cm × 3 cm |
| GDL thickness | 250 μm |
| GDL porosity | 0.7 |
| MEA thickness | 50 μm |

## 2. Theory and calculation

In this study, a commercial CFD solver, STAR-CD (CD-Adapco, Korea), with an add-on expert system, ES-PEMFC [22], was used to simulate the operation of PEMFCs. This program has been successfully used by many researchers for analyzing and designing flow fields and channel geometries for PEMFCs [23-25]. The ES-PEMFC solves coupled governing equations for mass conservation, energy conservation, and charge conservation by fully considering the detailed heat and mass transfer, fluid flow, and electrochemical reactions in PEMFCs.

In the ES-PEMFC module, two-phase flow model is used to consider the evaporation and condensation of water produced inside PEMFCs. In addition, the mass transfer resistance due to liquid water in GDLs is modeled by the existence of a thin water film covering PEMs, and the dissolution of gases into the water film is calculated by Henry's law. More detailed information regarding the ES-PEMFC methodology may be found in [22].

### *2.1 Computational model*

Fig. 1 shows three serpentine flow fields with one, three, and five parallel paths traveling over an active cell area of 9 $cm^2$ (3 cm × 3 cm). The detailed grid structure is also presented in Fig. 1(d), where the computational domain is divided into regions for a membrane electrode assembly (MEA, composed of a PEM and two CLs), GDLs, gas channels (GCs), and bipolar plates (BPs). The same flow field design was used for both anode and cathode reactant GCs to obtain co-flow configuration. The detailed geometric parameters for the flow field and channel designs are summarized in Table 1.

The number of finite volume cells was over 300,000 for the single serpentine flow field shown in Fig. 1(a). For parallel

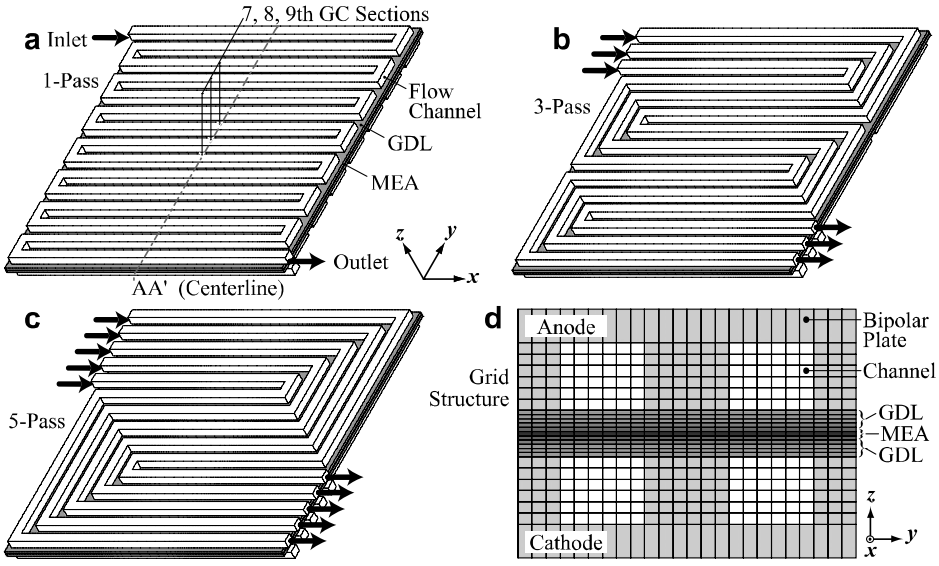


Fig. 1. Serpentine flow fields with (a) one, (b) three, and (c) five parallel paths for an active cell area of 9 $cm^2$, and (d) detailed grid structure.

Table 2. Governing equations and source terms.

| Governing equations | Mathematical expressions | |
|---|---|---|
| Mass conservation | $\frac{\partial(\rho u)}{\partial x}+\frac{\partial(\rho v)}{\partial y}+\frac{\partial(\rho w)}{\partial z}=s_m$ , where $s_m=s_{\mathrm{H}_2}$ (or $s_{\mathrm{O}_2}$) $+s^p_{\mathrm{H_2O},v}+s^e_{\mathrm{H_2O},v}$ . | T.1 |
| Momentum conservation | $u\frac{\partial(\rho u)}{\partial x}+v\frac{\partial(\rho u)}{\partial y}+w\frac{\partial(\rho u)}{\partial z}=-\frac{\partial p}{\partial x}+\frac{\partial}{\partial x}\left(\mu\frac{\partial u}{\partial x}\right)+\frac{\partial}{\partial y}\left(\mu\frac{\partial u}{\partial y}\right)+\frac{\partial}{\partial z}\left(\mu\frac{\partial u}{\partial z}\right)+s_{px}$ , | T.2 |
| | $u\frac{\partial(\rho v)}{\partial x}+v\frac{\partial(\rho v)}{\partial y}+w\frac{\partial(\rho v)}{\partial z}=-\frac{\partial p}{\partial y}+\frac{\partial}{\partial x}\left(\mu\frac{\partial v}{\partial x}\right)+\frac{\partial}{\partial y}\left(\mu\frac{\partial v}{\partial y}\right)+\frac{\partial}{\partial z}\left(\mu\frac{\partial v}{\partial z}\right)+s_{py}$ , | |
| | $u\frac{\partial(\rho w)}{\partial x}+v\frac{\partial(\rho w)}{\partial y}+w\frac{\partial(\rho w)}{\partial z}=-\frac{\partial p}{\partial z}+\frac{\partial}{\partial x}\left(\mu\frac{\partial w}{\partial x}\right)+\frac{\partial}{\partial y}\left(\mu\frac{\partial w}{\partial y}\right)+\frac{\partial}{\partial z}\left(\mu\frac{\partial w}{\partial z}\right)+s_{pz}$ , where | |
| | $s_{px}=-\frac{\mu}{K}u$ , $s_{py}=-\frac{\mu}{K}v$ , and $s_{pz}=-\frac{\mu}{K}w$ for GDL regions. | |
| Species conservation | $u\frac{\partial(\rho m_i)}{\partial x}+v\frac{\partial(\rho m_i)}{\partial y}+w\frac{\partial(\rho m_i)}{\partial z}=\frac{\partial(J_{x,i})}{\partial x}+\frac{\partial(J_{y,i})}{\partial y}+\frac{\partial(J_{z,i})}{\partial z}+s_i$ , where | T.3 |
| | $s_{\mathrm{H}_2}=-\frac{I(x,y)}{2F}M_{\mathrm{H}_2}A_{cv}$ at anode GDL/MEA interface, and | |
| | $s_{\mathrm{O}_2}=-\frac{I(x,y)}{4F}M_{\mathrm{O}_2}A_{cv}$ at cathode GDL/MEA interface. | |
| | $s_{\mathrm{H_2O}}=s^e_{\mathrm{H_2O},v}+s^p_{\mathrm{H_2O},v}$ , where | |
| | $s^e_{\mathrm{H_2O},v}=\frac{\alpha(x,y)}{F}I(x,y)M_{\mathrm{H_2O}}A_{cv}$ at anode GDL/MEA interface, or | |
| | $s^e_{\mathrm{H_2O},v}=\frac{1+2\alpha(x,y)}{2F}I(x,y)M_{\mathrm{H_2O}}A_{cv}$ at cathode GDL/MEA interface, and | |
| | $s_{\mathrm{H_2O},l}=-s^p_{\mathrm{H_2O},v}=-\frac{M_{\mathrm{H_2O}}\sum_{n\ \mathrm{of}\ v}\frac{mass_n}{M_n}}{1-p^{sat}_{\mathrm{H_2O},v}/p_v}\left[\frac{p^{sat}_{\mathrm{H_2O},v}-p_{\mathrm{H_2O},v}}{p_v}\right]\times r$ for fluid regions. | |
| Energy conservation | $\frac{\partial(\rho uh)}{\partial x}+\frac{\partial(\rho vh)}{\partial y}+\frac{\partial(\rho wh)}{\partial z}=\frac{\partial}{\partial x}\left(k\frac{\partial T}{\partial x}\right)+\frac{\partial}{\partial y}\left(k\frac{\partial T}{\partial y}\right)+\frac{\partial}{\partial z}\left(k\frac{\partial T}{\partial z}\right)+s^e_k+s^p_k$ , where | T.4 |
| | $s^e_k=I(x,y)\left[\frac{\Delta h_{form}}{2F}-V\right]A_{cv}$ at cathode GDL/MEA interface, and | |
| | $s^p_k=s_{\mathrm{H_2O},l}\times h_{fg}$ for fluid regions. | |

serpentine flow fields in Figs. 1(b) and 1(c), more than 400,000 finite volume cells were required. The calculation for the single serpentine flow field shown in Fig. 1(a) generally took about 10 h using a personal computer with a 1.86 GHz CPU.

### *2.2 Governing equations*

The governing equations required for the simulation of PEMFCs are summarized in Table 2. The major assumptions for the ES-PEMFC module are as follows [22]:

- Three-dimensional geometry for MEA, GCs, and BPs
- Steady-state and non-isothermal condition
- Laminar flow of incompressible Newtonian fluid
- Two-phase flow with evaporation/condensation of water
- Ideal gas mixture and Fickian diffusion
- Isotropic and homogeneous porous electrodes (GDLs)
- Negligible ohmic loss at GDLs and BPs

In Table 2, Eqs. T.1 and T.2 are the continuity and momentum equations, and Eq. T.3 is the species conservation equation expressed in terms of the species mass fraction, $m_i$ . Eqs. T.1-T.3 are solved for all fluid regions except solid regions for a PEM and BPs. In addition, the energy conservation equation of Eq. T.4 is solved for all regions, considering the conduction, convection, and heat source terms. Relevant source terms, $s$ , are also provided in Table 2. The mass generation and consumption terms due to the electrochemical reactions are defined at GDL/MEA interfaces.

In ES-PEMFC, the output voltage, $V$, of a PEMFC is determined as

$$V=V^{ocv}-IR(x,y)-\eta(x,y) \tag{1}$$

where $V^{ocv}$ denotes the open circuit voltage, $IR(x,y)$ denotes the ohmic loss, and $\eta(x,y)$ denotes the sum of the activation and concentration losses (termed as overpotential).

Table 3. Operating conditions.

| | | |
|---|---|---|
| Anode[a] | Inlet flow rate | 1.0 A/cm$^2$ equivalent |
| | Inlet temperature | 80°C |
| | Inlet due point | 80°C |
| | Mass fraction of $H_2$ | 0.115 |
| | Mass fraction of Water | 0.885 |
| | Exchange current density | 2000 A/m$^2$ |
| Cathode[a] | Inlet flow rate | 2.0 A/cm$^2$ equivalent |
| | Inlet temperature | 70°C |
| | Inlet dew point | 70°C |
| | Mass fraction of $O_2$ | 0.183 |
| | Mass fraction of water | 0.215 |
| | Exchange current density | 200 A/m$^2$ |
| PEMFC[a] | Open circuit voltage | 0.98 V |
| | Cell voltage | 0.6 V |
| | Inlet/outlet pressure | 1 atm |
| | Cell temperature | 70°C |
| Thermal conductivity[b] | MEA | 0.95 W/m-K |
| | GDL | 3.0 W/m-K |
| | Bipolar plate | 20 W/m-K |

[a] operating conditions are adopted from [23-25]
[b] thermal conductivity values are adopted from [26]

Table 4. Prescribed velocities at the inlets of flow channels.

| Number of paths | Anode GC | Cathode GC |
|---|---|---|
| 1 Path | 3.152 m/s | 11.25 m/s |
| 3 Paths | 1.051 m/s | 3.749 m/s |
| 5 Paths | 0.6303 m/s | 2.250 m/s |

Since the ohmic potential loss in a PEMFC mainly occurs inside the PEM, $IR(x,y)$ can be calculated in terms of the ionic conductivity, $\sigma_m$, as

$$IR(x,y) = I(x,y)\frac{t_m}{\sigma_m(x,y)} \tag{2}$$

where $t_m$ is the thickness of the PEM. Eq. (2) indicates that the ohmic loss is proportional to the current density, $I(x,y)$, while it is inversely proportional to the ionic conductivity of the PEM.

The overpotential, $\eta(x,y)$, is determined as a function of $I(x,y)$ and the partial pressure of oxygen, $p_{O_2}(x,y)$, and that of hydrogen, $p_{H_2}(x,y)$, at GDL/MEA interfaces, as

$$\eta(x,y) = \eta_c + \eta_a = \frac{RT(x,y)}{z_c F}\ln\left[\frac{I(x,y)}{I_{c,0}}\frac{p_{O_2}(x,y)}{p_{O_2,\infty}}\right] + \frac{RT(x,y)}{z_a F}\ln\left[\frac{I(x,y)}{I_{a,0}}\frac{p_{H_2}(x,y)}{p_{H_2,\infty}}\right] \tag{3}$$

where $R$ denotes the universal gas constant, $z_k$ denotes the number of electrons participating in the electrode reaction ($z_c = 4$ and $z_a = 2$), and $I_{k,0}$ denotes the exchange current density for the anode or the cathode. In addition, $p_{H_2,\infty}$ and $p_{O_2,\infty}$ are the partial pressures of hydrogen and oxygen at the channel inlets.

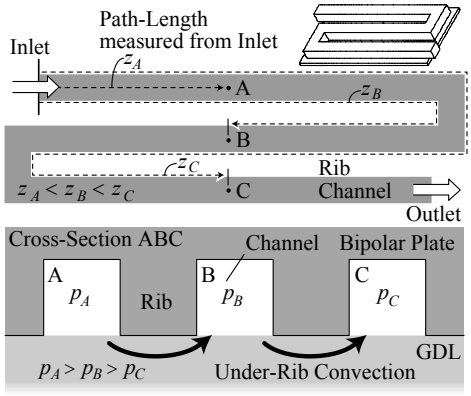


Fig. 2. Explanation of under-rib convection mechanism in a serpentine flow field.

### *2.3 Operating conditions*

The operating conditions for a PEMFC considered in the numerical simulations are summarized in Table 3. The hydrogen flow rate at the inlet of the anode GC was set to 1.0 A/cm$^2$ equivalent, while the air flow rate at the inlet of the cathode GC was set to 2.0 A/cm$^2$ equivalent. For sufficient humidification of the PEM, hydrogen and air were assumed to be fully humidified at the inlets of GCs. For cooling of the PEMFC, a prescribed temperature of 70°C was imposed on the top and the bottom boundaries of the anode and cathode BPs. The cell voltage was prescribed to be 0.6 V, while the open circuit voltage corresponding to the operating condition was 0.98 V.

The simulations were conducted for PEMFCs with 9 cm$^2$ active cell area. Three serpentine flow field designs shown in Figs. 1(a), 1(b) and 1(c) were considered as the reactant flow fields for both anode and cathode GCs. In addition, the permeability of GDLs was varied from $1\times10^{-12}$ to $1\times10^{-10}$ m$^2$ to investigate its impact on the performance of the PEMFC. Table 4 summarizes the inlet fluid velocities prescribed to simulate the serpentine flow fields. Note that higher fluid velocity is required as the number of parallel paths is increased.

### *2.4 Boundary conditions*

As the boundary conditions for the momentum and species conservation equations, the inlet conditions summarized in Table 3 and 4 were prescribed, along with the outflow conditions at the outlets. Then, the other boundaries were automatically treated as no-slip or impermeable walls in the ES-PEMFC module.

For the energy conservation equation, the temperature at the top boundary of the anode BP and the bottom boundary of the cathode GC was fixed at the cell temperature of 70°C (see Table 2), in addition to the inlet and outlet conditions. Similarly, the other boundaries were treated as adiabatic. Also note

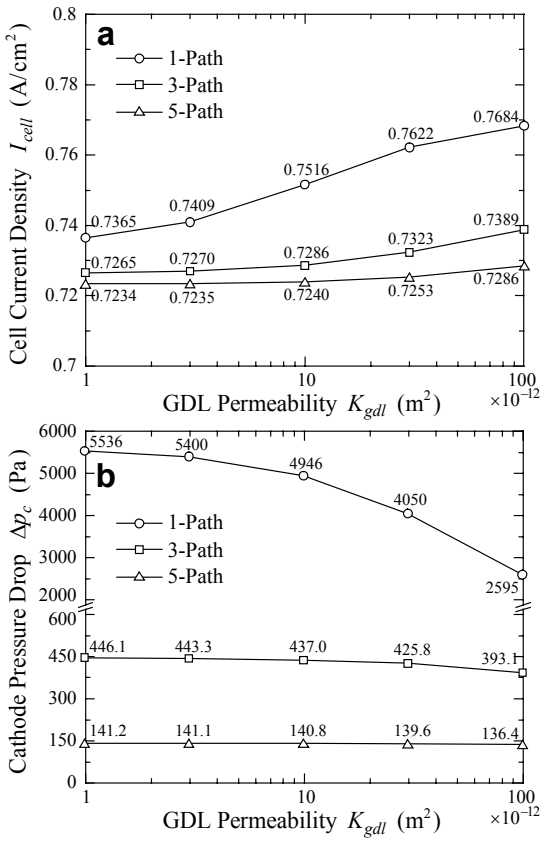


Fig. 3. Effects of GDL permeability on (a) the average current density, and (b) the cathode pressure drop in PEMFCs.

that the calculation of current density, $I(x, y)$, only requires the output voltage, $V$, as a boundary parameter.

## 3. Results and discussion

### *3.1 Under-rib convection mechanism*

As mentioned above, the ES-PEMFC module has been successfully used in many researches for the analysis of PEMFCs [23-25]. Thus, we did not perform validation studies for the ES-PEMFC module, by referring to the well documented validity results in the previous researches [23-25]. Instead, we focused more on the results and their discussion.

The under-rib convection mechanism is reviewed in Fig. 2 before inspecting the simulation results. A small region in a single serpentine flow field (1-path) is presented in Fig. 2. Note that a GC section, A, is in close contact with other two GC sections, B and C, which have different path-lengths, $z$, measured from the inlet. Because the pressure drop at a GC section is proportional to its path-length, $p_A > p_B > p_C$ holds for the three channel sections, A, B, and C, with $z_A < z_B < z_C$. The pressure difference between two adjacent GC sections causes convective flow through the under-rib paths of the porous GDL, as indicated in Fig. 2, which is called under-rib convection.

The merits of enhanced convective flow in the under-rib regions of GDLs are also well understood by Fig. 3. The under-rib convection increases the reactant concentration near CLs and, at the same time, decreases the product concentration by enhancing gas transport rate. In addition, it can help reduce the electrode flooding by facilitating water exhaust from the under-rib regions of GDLs [18, 19]. Higher reactant concentration enhances the electrochemical reaction at CLs while lower electrode flooding increases mass transport rate at GDLs. Thus, better performance of PEMFCs is generally expected with a higher under-rib convection intensity in GDLs.

### *3.2 Overall performance variation*

Fig. 3 summarizes the overall performance of a PEMFC simulated with different flow field designs and different permeability values for GDLs. The cell current density, $I_{cell}$, in Fig. 3(a) was obtained by averaging local current density over the active cell area. And the cathode pressure drop, $\Delta p_c$, in Fig. 3(b) was calculated by the pressure difference between the inlet and the outlet of the cathode GC. Fig. 3(a) indicates that single serpentine flow fields (1-path) lead to higher cell current density compared with parallel serpentine flow fields (3-path and 5-path). It is also found that higher permeability of GDLs generally improves the average current density of PEMFCs.

In Fig. 3(a), the performance enhancement due to increased GDL permeability is more noticeable for the single serpentine flow field (1-path) than for the parallel serpentine flow fields (3-path and 5-path). For example, the cell current density is enhanced by about 0.032 A/cm$^2$ (4.3%) for the single serpentine flow field during the GDL permeability increase from $1\times10^{-12}$ m$^2$ to $1\times10^{-10}$ m$^2$, while those for the parallel serpentine flow fields are enhanced by about 0.012 A/cm$^2$ (3-path) or about 0.005 A/cm$^2$ (5-path). In summary, increasing GDL permeability has more influence on the PEMFC performance when the number of parallel paths in the serpentine flow field is smaller. These performance trends may be explained by referring to the under-rib convection effect in serpentine flow fields.

In general, single serpentine flow fields, such as the one shown in Fig. 1(a), result in higher under-rib convection intensity due to the close contact of GC sections with different path-lengths, $z$. In contrast, adjacent GC sections in parallel serpentine flow fields have similar path-lengths as observed in Figs. 1(b) and 1(c), which leads to low under-rib convection intensity in those flow fields. Therefore, the observed better performance of PEMFCs with the single serpentine flow field can be attributed to higher under-rib convection intensity. Because of the same under-rib convection effect, the cell current density for the single serpentine flow field becomes more sensitive to the permeability of GDLs. With higher GDL permeability, convective flow in the under-rib regions of GDLs is facilitated more, which in turn enhances the performance of PEMFCs.

The cathode pressure drop shown in Fig. 3(b) also supports the explanation based on the under-rib convection effect. The

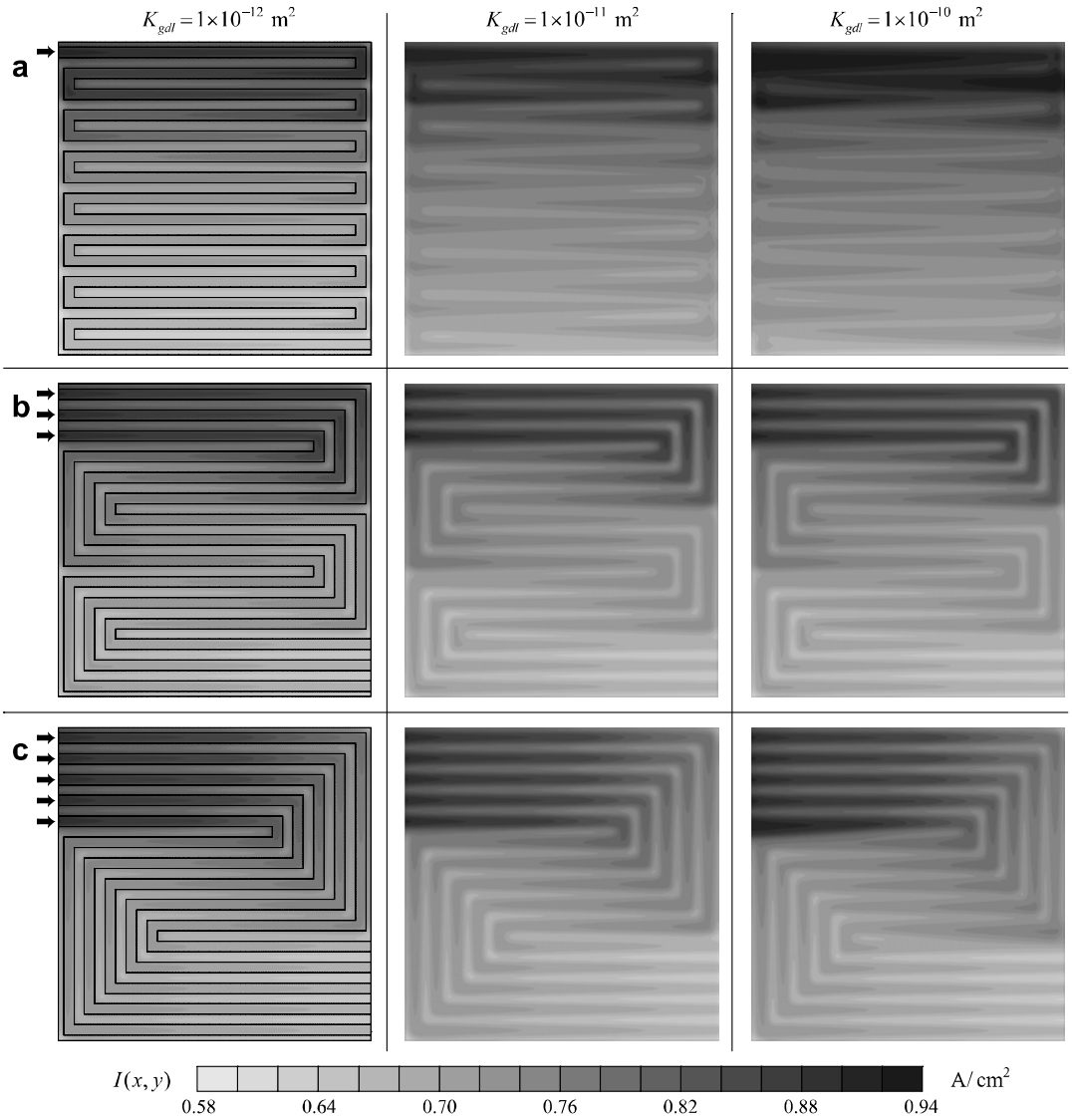


Fig. 4. Local current density distribution for serpentine flow fields with (a) one, (b) three, and (c) five parallel paths. The GDL permeability is varied as $1.0\times10^{-12}$, $1.0\times10^{-11}$, and $1.0\times10^{-10}$ m$^2$.

pressure drop across the cathode GC of the single serpentine flow field is significantly reduced from about 5536 Pa for $K_{gdl} = 1\times10^{-12}$ m$^2$ to about 2595 Pa for $K_{gdl} = 1\times10^{-10}$ m$^2$. The under-rib convection in the single serpentine flow field decreases the amount of gas that flows through the GC, leading to such large reduction in the pressure drop. In contrast, for parallel serpentine flow fields with negligible under-rib convection, the cathode pressure drop is only slightly reduced during the 100-fold increase in the GDL permeability.

Fig. 3(b) also shows that $\Delta p_c$ is much smaller for the parallel serpentine flow fields (3-path and 5-path) than for the single serpentine flow field (1-path). This is because both the channel path-length and the gas flow rate in each path are inversely proportional to the number of parallel paths, $N_{path}$. In addition, the secondary pressure drop at many curved GC sections in serpentine flow fields is also dependent on the square of flow speed. In summary, the cathode pressure drop, $\Delta p_c$, shown in Fig. 3(b) has a dependency of $\Delta p_c \sim N_{path}^{-2.282}$ for $K_{gdl} = 1\times10^{-12}$ m$^2$, where the coefficient of determination, $r^2$, is close to 1.

At this moment, it is worth noting that the superior cell performance of the single serpentine flow field shown in Fig. 3(a) may not directly lead to a better system performance. This is because the overall performance of a PEMFC system is also influenced by the parasitic power consumption for operating auxiliary devices of the system, such as pumps, blowers, or compressors. Thus, in some cases, the better cell performance of the single serpentine flow field can be offset by higher pumping power due to the more severe pressure drop shown in Fig. 3(b), resulting in negligible enhancement or even degradation of the system performance.

Fig. 4 presents the spatial distribution of local current den-

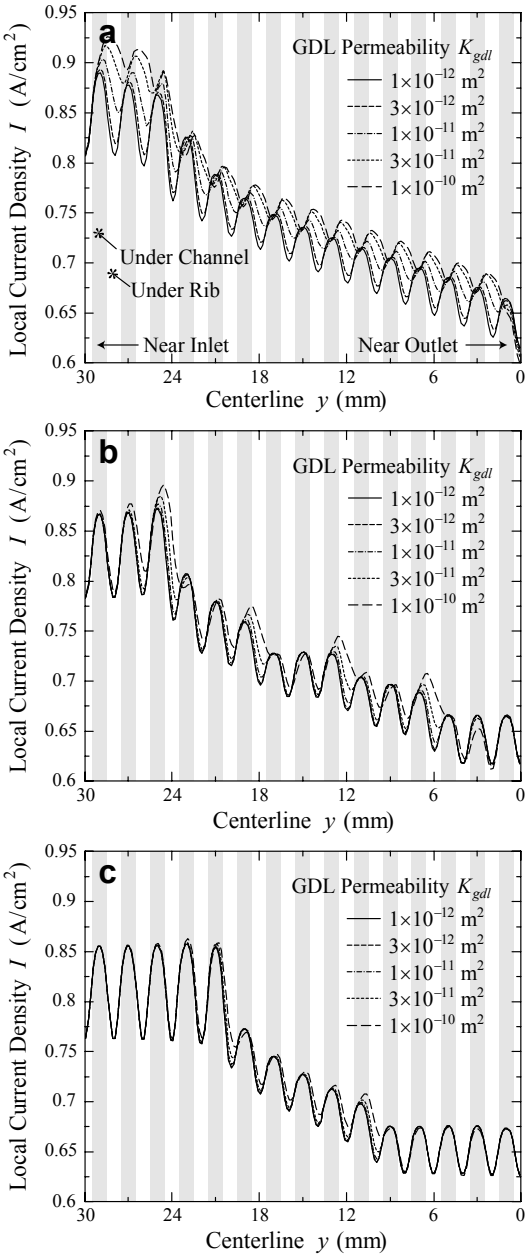


Fig. 5. Local current density distribution along the centerline for serpentine flow fields with (a) one (1-path), (b) three (3-path), and (c) five parallel paths (5-path).

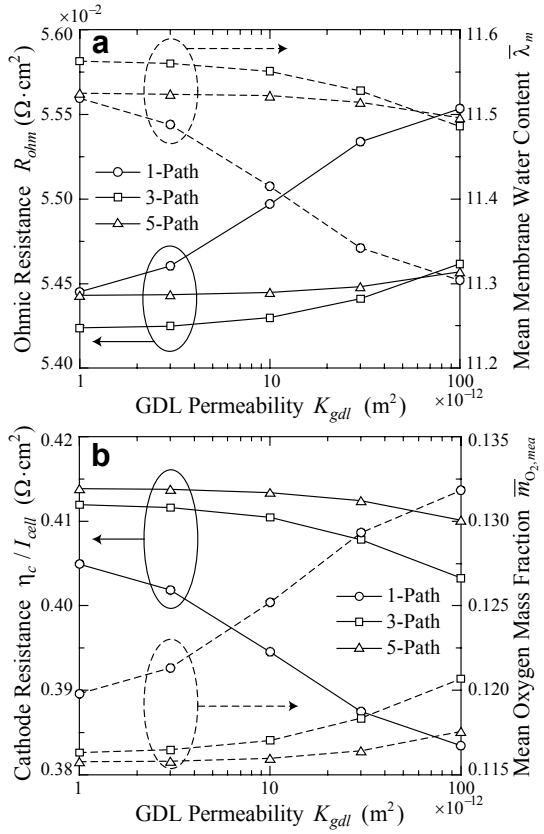


Fig. 6. Effects of GDL permeability on (a) the cell ohmic resistance and (b) the cell cathode resistance. The mean water content of membrane and the mean oxygen concentration at cathode MEA are also presented.

sity, $I(x,y)$, in the square active area of 3 cm × 3 cm. Note that the local current density at the anode-side of MEA is almost the same as that at the cathode-side due to the small thickness of the membrane. In Fig. 4, the locations of channel and rib boundaries are indicated by thin solid lines. It is found that the highest local current density is obtained at the under-channel regions near the inlets where the reactant concentrations are high. On the other hand, the lowest local current density is found at the under-rib regions near the outlets, especially when GDL permeability is small as $K_{gdl} = 1\times10^{-12}$ m$^2$.

In Figs. 4(b) and 4(c) for the parallel serpentine flow fields, the distribution of local current density is not much influenced by the variation in GDL permeability. The magnitude of local current density is always higher in the under-channel regions than in the under-rib regions, by which the flow field patterns are clearly identified. In contrast, the current density distribution for the single serpentine flow field is found to significantly alter as GDL permeability is increased. In Fig. 4(a), local current density is generally higher in the under-channel regions for $K_{gdl} = 1\times10^{-12}$ m$^2$, which is similar to the parallel flow field cases shown in Figs. 4(b) and 4(c). However, when GDL permeability increases to $1\times10^{-11}$ m$^2$ or $1\times10^{-10}$ m$^2$, local current density in the under-rib regions becomes higher than that in the under-channel regions, thereby resulting in 'zig-zag' patterns shown in Fig. 4(a).

Close inspection of Fig. 4(a) for $K_{gdl} = 1\times10^{-11}$ m$^2$ and $1\times10^{-12}$ m$^2$ indicates that higher local current density is obtained in the under-rib regions near the corners of the single serpentine flow fields. This result may be explained by the fact that the convection intensity in an under-rib region is dependent on the difference in path-length, $\Delta z$, between two GC sections (see Fig. 2). Thus, under-rib regions along the centerline of serpentine flow fields have a path-length difference of $\Delta z = l_x$, where $l_x$ denotes the length of the active cell in the $x$-direction. In contrast, under-rib regions near the

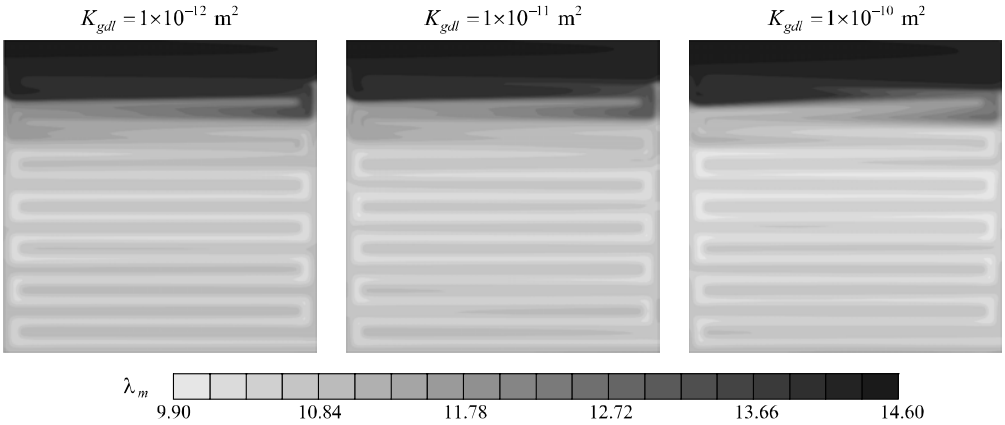


Fig. 7. Distribution of membrane water content for single serpentine flow field ($K_{gdl}$= 1.0×10$^{-12}$, 1.0×10$^{-11}$, and 1.0×10$^{-10}$ m$^2$).

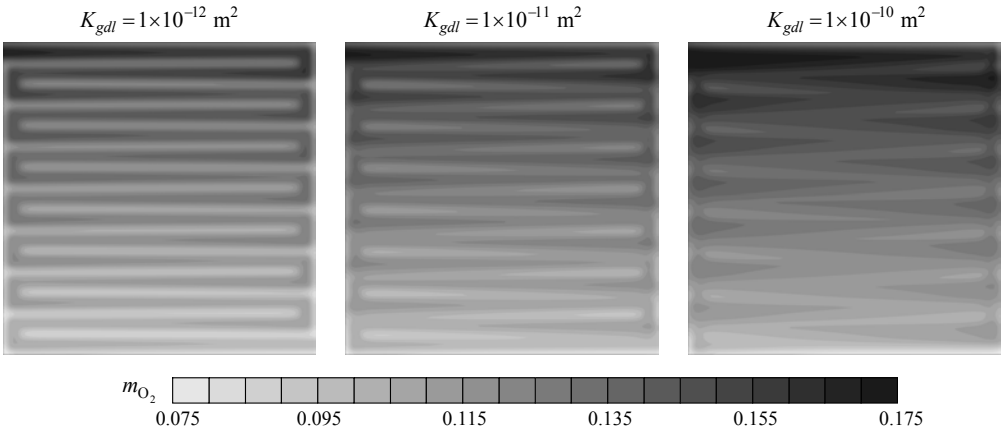


Fig. 8. Distribution of oxygen concentration at cathode MEA for single serpentine flow field ($K_{gdl}$= 1.0×10$^{-12}$, 1.0×10$^{-11}$, and 1.0×10$^{-10}$ m$^2$).

corners of serpentine flow fields have a larger path-length difference of $\Delta z = 2l_x$, and thus the under-rib convection intensity is higher there. The enhancement of local current density due to such under-rib convection effects is also observed in some regions with larger path-length differences in Figs. 4(b) and 4(c) for the parallel serpentine flow fields.

For more quantitative analysis of the results, the distribution of local current density along the centerline of the flow fields is plotted in Fig. 5 (find the definition of the centerline AA' in Fig. 1). Fig. 5 clearly indicates that the variation in GDL permeability has higher impacts on the single serpentine flow field than on the parallel serpentine flow fields, which is consistent with the results found in Figs. 3 and 4. In Figs. 5(b) and 5(c) for the parallel serpentine flow fields, higher local current density is generally obtained in the under-channel regions compared to the nearby under-rib regions, regardless of GDL permeability. However, a different trend is observed for the single serpentine flow field shown in Fig. 5(a). Local maximums for current density are obtained in the under-channel regions when GDL permeability is small as 1×10$^{-12}$ m$^2$ or 3×10$^{-12}$ m$^2$, but their positions move towards the under-rib regions as GDL permeability increases towards 1×10$^{-10}$ m$^2$. It should be noted that under-rib convection intensity is believed to be smaller along the centerline in the middle of the single serpentine flow field, compared to that near the corners of the flow field.

Fig. 6 summarizes the effects of GDL permeability on cell ohmic resistance, $R_{ohm}$, and overall cathode resistance, $\eta_c / I_{cell}$. Fig. 6(a) indicates that mean water content, $\overline{\lambda}_m$, in the membrane decreases with increase in GDL permeability, resulting in higher ohmic resistances. However, the variation in the cell ohmic resistance shown in Fig. 6(a) is, in fact, small considering the 100-fold increase of GDL permeability from 1×10$^{-12}$ m$^2$ to 1×10$^{-10}$ m$^2$. The increase of $R_{ohm}$ amounts to only about 1.8%, 0.7%, and 0.3% for the serpentine flow fields with one, three, five parallel paths, respectively. The under-rib convection effect can explain the increase of ohmic resistance with GDL permeability as follows. Higher under-rib convection intensity facilitates the exhaust of water vapor (product) out of the GDL. This results in a smaller vapor pressure near MEA, leading to a smaller equilibrium water content in the membrane.

In Fig. 6(b), mean oxygen concentration at the cathode-side of MEA, $\overline{m}_{O_2,MEA}$, is found to increase by about 10% (1-path), 3.8% (3-path), and 1.5% (5-path) when GDL permeability is increased from 1×10$^{-12}$ m$^2$ to 1×10$^{-10}$ m$^2$. Accordingly, overall cathode resistance is decreased by about 5.3%, 2.1% and 0.9% for the serpentine flow fields with one, three,

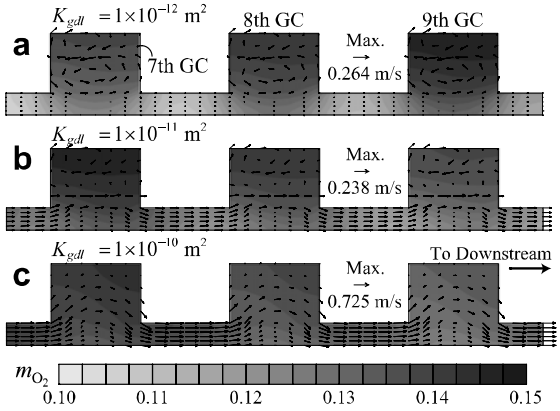


Fig. 9. Cross-sectional views of transversal velocity and oxygen concentration in three GC and GDL sections for (a) $K_{gdl}$= $1\times10^{-12}$ m$^2$, (b) $1\times10^{-11}$ m$^2$, and (c) $1\times10^{-10}$ m$^2$.

five parallel paths, respectively. Thus, Fig. 6(b) indicates that the obtained better performance with higher GDL permeability is largely due to the increase in the reactant concentration near the MEA. Higher under-rib convection enhances mass transport rates required for supplying reactant to and removing product out of the MEA.

The local distribution of membrane water content is presented in Fig. 7 for the single serpentine flow field. In Fig. 7, $\lambda_m$ exhibits only slight reduction in magnitude as GDL permeability increases, but the magnitude is less noticeable as inferred from Fig. 6(a). Fig. 8 shows the local distribution of oxygen mass fraction at the cathode-side of the MEA. Note the close similarity between Fig. 8 for oxygen concentration distribution and Fig. 4(a) for current density distribution. In Fig. 8, the oxygen concentration is generally higher in the under-channel regions than in the under-channel region for $K_{gdl} = 1\times10^{-12}$ m$^2$. However, oxygen concentration also exhibits a 'zig-zag' pattern due to active under-rib convection when GDL permeability is $1\times10^{-10}$ m$^2$. The resemblance between the oxygen concentration and current density distributions clearly indicates the importance of under-rib convection for the performance of PEMFCs with serpentine flow fields.

Finally, a transversal velocity field ($y$ and $z$ components) for three adjacent GC and GDL sections is shown in Fig. 9, along with the distribution of oxygen concentration. For the exact location of the GC sections shown in Fig. 9, please refer to Fig. 1. In Fig. 9, the magnitude of under-rib convection velocity is negligible for $K_{gdl} = 1\times10^{-12}$ m$^2$, but increases to about 0.2 m/s for $K_{gdl} = 1\times10^{-11}$ m$^2$ and to about 0.7 m/s for $K_{gdl} = 1\times10^{-10}$ m$^2$. According to the under-rib convection enhancement, oxygen concentration near the cathode-side of MEA becomes more uniform among the under-channel regions and the under-rib regions. It is interesting that the transversal flow patterns in the GC sections are also influenced by the under-rib convection intensity. In Fig. 9(c), the highest oxygen concentration is obtained at the edges of GC sections towards downstream direction.

At this moment, it may be worthwhile to review actual permeability values of GDL materials used in PEMFCs. Williams et al. [15] reported the through-plane permeability of several GDL materials and obtained $8.7\times10^{-12}$ m$^2$ for a bare Toray carbon paper (TGP-H-120) with 75.6% porosity, and $1.9\times10^{-12}$ m$^2$ for the same paper after a microporous layer application. Feser et al. [17] reported the in-plane permeabilities of several carbon paper media for GDLs, including the compression effect; the in-plane permeability of a Toray carbon paper (TGP-H-60) was measured to be about $1.1\times10^{-11}$ m$^2$ at 77% porosity when it was compressed to about 96% of the initial thickness (about 96% compression ratio), but the in-plane permeability reduced to about $5.0\times10^{-12}$ m$^2$ at 71% porosity (corresponding to about 70% compression ratio). Feser et al. [17] also showed that the in-plane permeability of SGL carbon paper (SGL31BA) amounted to about $4.3\times10^{-11}$ m$^2$ at 78.5% porosity (about 87% compression ratio) and about $2.2\times10^{-11}$ m$^2$ at 75% porosity (about 77% compression ratio). In the present numerical simulations, GDL permeability was varied from $1\times10^{-12}$ m$^2$ to $1\times10^{-10}$ m$^2$. Thus, the range of $K_{gdl}$ considered in this study is believed to appropriate.

## 4. Conclusions

The correlation between the permeability of GDLs and the performance of PEMFCs with serpentine flow fields was numerically investigated in this study. The serpentine flow fields were made to have one, three, and five parallel paths, while the GDL permeability was varied from $1\times10^{-12}$ m$^2$ to $1\times10^{-10}$ m$^2$. From the numerical simulations, PEMFCs with single serpentine flow fields (1-path) were found to have better performance than PEMFCs with parallel serpentine flow fields (3-path and 5-path) for the same GDL permeability. This result was explained by the fact that higher convection intensity is induced in under-rib regions of GDLs due to larger path-length difference in single serpentine flow fields.

The numerical simulations also showed that higher permeability of GDLs was advantageous for the performance of PEMFCs, especially when single serpentine flow fields were employed as reactant flow fields. The current density distribution showed that higher current density was obtained in under-channel regions of single serpentine flow fields when GDL permeability was small. However, as GDL permeability increased, the position of local maxima of current density moved towards under-rib regions, which pointed to the importance of under-rib convection in enhancing the performance of PEMFCs.

For more detailed study on under-rib convection effects, we investigated the distribution of membrane water content and oxygen concentration at the cathode-side of MEA. We found that oxygen concentration was greatly increased with higher GDL permeability, while membrane water content was less sensitive. In addition, a similarity between the distribution of current density and that of oxygen concentration was clearly observed. Therefore, higher reactant concentration near reaction sites due to enhanced under-rib convection intensity was

indentified to be the key reason for the performance enhancement of PEMFCs with higher GDL permeability.

## Acknowledgment

This work was supported by the second stage of the Brain Korea 21 (BK21) Project in 2010, and by the National Research Foundation of Korea (NRF) funded by the Ministry of Education, Science and Technology (2010-0012613). The authors are also grateful to CD-Adapco, Korea for allowing us to use STAR-CD and ES-PEMFC module (an add-on expert system for PEMFC).

## Nomenclature

$A$ : Active reaction area, $m^2$
$F$ : Faraday constant, 96,485 C/mol
$h$ : Enthalpy, J
$h_{fg}$ : Enthalpy of vaporization, J
$\Delta h_{form}$ : Enthalpy of formation, J
$I$ : Current density, $A/cm^2$
$J_i$ : Mass flux of species $i$, $kg/m_2$-s
$K_{gdl}$ : GDL permeability, $m^2$
$M_i$ : Molecular mass of species $i$, kg/mol
$m_i$ : Mass fraction of species $i$
$mass_n$ : Mass of species $n$, kg
$p_i$ : Partial pressure of species $i$, Pa
$R_{ohm}$ : Cell ohmic resistance, $\Omega$-$cm^2$
$s$ : Source term
$T$ : Temperature, K
$z$ : Channel path-length, m

### *Greek letters*

$\alpha$ : Effective electro-osmosis coefficient
$\varepsilon$ : Porosity
$\eta$ : Overpotential, V
$\lambda_m$ : Membrane water content
$\sigma_m$ : Ionic conductivity of membrane, S/m

Superscripts/subscripts
*a/c* : Anode/cathode
*e/p* : Electrochemical/phase change
*gdl* : Gas diffusion layer
*l/v* : Liquid/vapor
*sat* : Saturation

## References

[1] J. Larminie and A. Dicks, *Fuel Cell Systems Explained*, 2nd Edition, John Wiley & Sons, New York (2003).
[2] R. O'Hayre, S. W. Cha, W. Colella and F. B. Prinz, *Fuel Cell Fundamentals*, John Wiley & Sons, New York (2005).
[3] A. Faghri and Z. Guo, Challenges and opportunities of thermal management issues related to fuel cell technology and modeling, *International Journal of Heat and Mass Transfer*, 48 (2005) 3891-3920.
[4] H. Li, Y. H. Tang, Z. W. Wang, Z. Shi, S. H. Wu, D. T. Song, J. L. Zhang, K. Fatih, J. J. Zhang, H. J. Wang, Z. S. Liu, R. Abouatallah and A. Mazza, A review of water flooding issues in the proton exchange membrane fuel cell, *Journal of Power Sources*, 178 (2008) 103-117.
[5] N. Yousfi-Steiner, Ph. Moçotéguy, D. Candusso, D. Hissel, A. Hernandez and A. Aslanidesa, A review on PEM voltage degradation associated with water management: Impacts, influent factors and characterization, *Journal of Power Sources*, 183 (2008) 260-274.
[6] C. Xu and T. S. Zhao, A new flow field design for polymer electrolyte-based fuel cells, *Electrochemistry Communications*, 9 (2007) 497-503.
[7] X. D. Wang, Y. Y. Duan, W. M. Yan and X. F. Peng, Local transport phenomena and cell performance of PEM fuel cells with various serpentine flow field designs, *Journal of Power Sources*, 175 (2008) 397-407.
[8] J. Choi, Y. H. Kim, Y. Lee, K. J. Lee and Y. Kim, Numerical analysis on the performance of cooling plates in a PEFC, *Journal of Mechanical Science and Technology*, 22 (2008) 1417-1425.
[9] J. H. Nam, K. J. Lee, S. Sohn and C. J. Kim, Multi-pass serpentine flow-fields to enhance under-rib convection in polymer electrolyte membrane fuel cells: Design and geometrical characterization, *Journal of Power Sources*, 188 (2009) 14-23.
[10] T. V. Nguyen, A gas distributor design for proton-exchange-membrane fuel-cells, *Journal of the Electrochemical Society*, 143 (1996) L103-L105.
[11] W. He, J. S. Yi and T. V. Nguyen, Two-phase flow model of the cathode of PEM fuel cells using interdigitated flow fields, *AIChE Journal*, 46 (1999) 2053-2064.
[12] S. Dutta, S. Shimpalee and J. W. Van Zee, Numerical prediction of mass-exchange between cathode and anode channels in a PEM fuel cell, *International Journal of Heat and Mass Transfer*, 44 (2001) 2029-2042.
[13] P. H. Oosthuizen, L. Sun and K. B. McAuley, The effect of channel-to-channel gas crossover on the pressure and temperature distribution in PEM fuel cell flow plates, *Applied Thermal Engineering*, 25 (2005) 1083-1096.
[14] J. Park and X. Li, An experimental and numerical investigation on the cross flow through gas diffusion layer in a PEM fuel cell with a serpentine flow channel, *Journal of Power Sources*, 163 (2007) 853-862.
[15] M. V. Williams, H. R. Kunz and J. M. Fenton, Influence of convection through gas-diffusion layers on limiting current in PEMFCs using a serpentine flow field, *Journal of the Electrochemical Society*, 151 (2004) A1617-A1627.
[16] J. G. Pharoah, On the permeability of gas diffusion media used in PEM fuel cells, *Journal of Power Sources*, 144 (2005) 77-82.
[17] J. P. Feser, A. K. Prasad and S. G. Advani, On the relative influence of convection in serpentine flow fields of PEM fuel cells, *Journal of Power Sources*, 161 (2006) 404-412.

[18] T. Kanezaki, X. Li and J. J. Baschuk, Cross-leakage flow between adjacent flow channels in PEM fuel cells, *Journal of Power Sources*, 162 (2006) 415-425.
[19] K. B. S. Prasad and S. Jayanti, Effect of channel-to-channel cross-flow on local flooding in serpentine flow-fields, *Journal of Power Sources*, 180 (2008) 227-231.
[20] Q. Ye, T. S. Zhao and C. Xu, The role of under-rib convection in mass transport of methanol through the serpentine flow field and its neighboring porous layer in a DMFC, *Electrochimica Acta*, 51 (2006) 5420-5429.
[21] D. H. Ahmed, H. J. Sung and J. Bae, Effect of GDL permeability on water and thermal management in PEMFCs - I. Isotropic and anisotropic permeability, *International Journal of Hydrogen Energy*, 33 (2008) 3767-3785.
[22] *STAR-CD: ES-PEMFC Methodology and Tutorial Manual*, CD-Adapco Group.
[23] S. Shimpalee, S. Greenway and J. W. Van Zee, The impact of channel path length on PEMFC flow-field design, *Journal of Power Sources*, 160 (2006) 398-406.
[24] S. Shimpalee and J. W. Van Zee, Numerical studies on rib & channel dimension of flow-field on PEMFC performance, International Journal of Hydrogen Energy, 32 (2007) 842-856.
[25] D. H. Jeon, S. Greenway, S. Shimpalee and J. W. Van Zee, The effect of serpentine flow-field designs on PEM fuel cell performance, *International Journal of Hydrogen Energy*, 33 (2008) 1052-1066.
[26] Y. Wang and C. Y. Wang, Two-phase transients of polymer electrolyte fuel cells, *Journal of the Electrochemical Society*, 154 (2007) B636-B643.

**Seung Man Baek** received his B.S. in Mechanical Engineering from Seoul National University of Technology, Korea, in 2005. Then, he received the M.S. in Mechanical Engineering from Seoul National University, Korea, in 2007. Currently, he is a Ph.D. candidate in the School of Mechanical and Aerospace Engineering at Seoul National University. His research is focused on the thermal modeling of Li-ion battery systems, fuel cell systems, and solar thermal systems.

**Charn-Jung Kim** received his B.S. and M.S. in Mechanical Engineering from Seoul National University, Korea, in 1983 and 1985, respectively. Then, he received Ph.D. in Mechanical Engineering from the University of Michigan in 1991. Dr. Kim currently works as an associate Professor at School of Mechanical and Aerospace Engineering at Seoul National University. His research interests are focused on the numerical methods for thermo-fluid processes including computational fluid dynamics, heat and mass transfer, phase-change materials, and fuel cell systems.